The interaction of crossover formation and the dynamic architecture of the synaptonemal complex during meiosis

Simone Köhler[1,2,*], Michal Wojcik[3,4,*], Ke Xu[3,4,5,6,#] and Abby F. Dernburg[1,2,5,7,#]

1. Department of Molecular and Cell Biology, University of California, Berkeley, Berkeley CA 94720-3220
2. Howard Hughes Medical Institute, 4000 Jones Bridge Road, Chevy Chase, MD 20815
3. Department of Chemistry, University of California, Berkeley, Berkeley CA 94720-3220
4. Chan Zuckerberg Biohub, San Francisco, CA 94158, USA
5. California Institute for Quantitative Biosciences, Berkeley CA 94720
6. Division of Molecular Biophysics and Integrated Bioimaging, Lawrence Berkeley National Laboratory, Berkeley, CA 94720
7. Division of Biological Systems and Engineering, Lawrence Berkeley National Laboratory, Berkeley CA 94720

* these authors contributed equally to this work.
# corresponding authors:
Ke Xu <xuk@berkeley.edu>
Abby F. Dernburg < afdernburg@berkeley.edu >

1

25 **During meiosis, chromosomes pair with their homologous partners, and a structure known**

26 **as the synaptonemal complex (SC) assembles between them. Evidence indicates that this**

27 **material plays a role in regulating crossover recombination between homologs, although**

28 **this remains controversial. Here we use three-dimensional STochastic Optical**

29 **Reconstruction Microscopy (3D-STORM) to interrogate the molecular architecture of the**

30 **SC in intact germline tissue from *Caenorhabditis elegans*, and analyze its ultrastructure**

31 **during meiotic progression. Using a probabilistic mapping approach, we determine the**

32 **position and orientation of the four known SC structural proteins. We report that a**

33 **marked structural transition occurs within this material upon crossover designation. We**

34 **also identify a mutation that disturbs both SC ultrastructure and crossover interference,**

35 **the widespread mechanism that results in non-randomly wide spacing of crossovers**

36 **between the same chromosome pair. Together with other evidence, our findings suggest**

37 **that the SC is an active material, and that structural transitions may directly contribute to**

38 **chromosome-wide crossover regulation.**

39

40 The synaptonemal complex (SC) is a protein structure that assembles between homologous

41 chromosomes during meiotic prophase, stabilizing their parallel alignment [1]. The SC appears

42 as a periodic ladder-like structure in electron micrographs [2]. Recent studies have revealed that

43 this material shows dynamic, liquid-like behavior [3-7]. The SC is required for and appears to

44 regulate meiotic recombination [3, 8-13]. Despite its central role in meiosis, the molecular

45 organization of the SC remains poorly characterized.

46

47 In *C. elegans,* the SC assembles between homologs even in the absence of meiotic recombination

48 [14]. Four structural proteins essential for SC assembly have been identified: SYP-1, SYP-2,

49 SYP-3, and SYP-4 [15-18]. Limited information about their organization within the SC has been

50 obtained through protein-protein interaction analysis and immuno-electron microscopy [19].

51 Super-resolution microscopy has emerged as a powerful tool to investigate the organization of

52 macromolecular assemblies, including the SC [20, 21]. We recently described the molecular

53 architecture of meiotic chromosome axes, which form the substrate for SC assembly, based on

54 3D-STORM [22, 23] in intact *C. elegans* gonads [24]. Here, we apply this approach to analyze

55 the organization of the SC during meiotic prophase.

2

Results

57 Using antibodies that bind either short peptides within SC proteins or epitope tags inserted by

58 genome editing, we localized the SYP proteins along paired meiotic chromosomes using 3D-

59 STORM and averaging methods (Extended Data Fig. S1). The orientation of the SC in our

60 images was defined by labeling a reference protein in the chromosome axes, HIM-3 [25]. For

61 positional mapping of SC proteins, we analyzed regions that were observed in frontal view (Fig.

62 1b, c). We rotated all images about the optical axis (z-axis) such that the chromosomes are

63 extended along the y-axis, with the SC spanning the distance between the homologs on the x-axis

64 (Extended Data Fig. S1b-c, methods). Taking advantage of the well-characterized progression of

65 meiotic stages within the germline of adult *C. elegans*, we compared SC organization before,

66 during and after the designation of crossover sites (Fig. 1a).

67

Dynamic architecture of the synaptonemal complex in *C. elegans*

69 The width of the SC in *x* in *C. elegans*, as measured from electron micrographs, is

70 approximately 96 nm [3]. An antibody recognizing the C-terminal peptide of SYP-1 was

71 resolved as two parallel strands, located at 42.3±0.8 nm and 42.0±1.2 nm off-center in early and

72 late pachytene, respectively (Fig. 1b, m). This epitope thus lies near the outer edges of the SC

73 and within a few nanometers of HIM-3, the most proximal known component of the

74 chromosome axis (Table S1)[24]. Intriguingly, in cross-sectional views (xz-view, Fig. 1c) we

75 observed striking differences in its distribution in z between early and late pachytene SCs: While

76 the C-terminus of SYP-1 was confined near the central plane in early pachytene, it was widely

77 distributed in z in late pachytene (Fig. 1d, e, m, center and Table S1).

78 We then asked whether the N-terminus of SYP-1 is similarly relocalized during meiotic

79 progression. Tagging the N-terminus of SYP-1 disrupts SC assembly ([26] and data not shown),

80 but we identified a poorly conserved region close to the N-terminus in which insertion of an HA

81 epitope did not impair function (Table S2). Interestingly, this epitope was confined to a thin

82 plane in the center of the SC along both the *x* and *z* axis in both early and late pachytene SCs

83 (Fig. 1d, e, m, top). Our data support a transverse orientation for SYP-1, as previously reported

84 [19], with its N-terminus at the center and C-terminus near the axes. Thus, SYP-1 appears to be

85 an ortholog of "transverse filament" proteins from other organisms [27-31]. Importantly, these

86 localization data are inconsistent with a uniform growth in thickness of the SC through e.g.

3

87   lateral stacking of SYP-1 molecules during meiotic progression, which has previously been

88   suggested based on observations of increased fluorescence intensity during late pachytene in

89   budding yeast [4] and *C. elegans* [5]. The distinct localization patterns of N- and C-terminal

90   epitopes in early and late SCs along the *z* axis suggest a more complex reorganization of SYP-1

91   during meiosis.

92   To further probe the orientation of SYP-1 within the SC, we mapped the N-terminal

93   localization events to the C-terminal distributions, assuming a rigid, rod-like conformation (Fig.

94   S2a-b, see methods). Our approach indicated that SYP-1 lies nearly parallel to the SC in early

95   pachytene, but is diagonally oriented in late pachytene (Fig. 2a-b).

96   We next asked how the organization of other SC components was affected by meiotic

97   progression. We mapped the C-termini of SYP-2, SYP-3-HA and SYP-4-HA, the N-terminus of

98   GFP-SYP-3[32], and an epitope inserted into the middle of SYP-4 (Table S2, Fig. 1d, e, m and

99   Extended Data Fig. S3). The results are summarized in Table S1. We observed consistent

100   differences between early and late pachytene for most epitopes, particularly for the C-terminus of

101   SYP-4, which moves from a central plane in early pachytene to a splayed orientation, protruding

102   above and below the central plane of the SC, in late pachytene (Fig. S2c and S3, Table S1).

103   Similarly, epitopes on SYP-2 and SYP-3 were more central in early pachytene than late

104   pachytene (Fig. 1d,e,m, S2c and Fig. S3). We further found that SYP-3 localized at (N) or close

105   to (C) the midline of the SC in *x*, suggesting a head-to-head arrangement of SYP-3 molecules

106   (Fig. S3 and Table S1). These findings are inconsistent with one conclusion of a previous study,

107   that the C-terminus of SYP-3 lies in proximity to the axes [19]. This discrepancy may reflect the

108   challenges of determining the orientation of the SC in samples prepared for immuno-EM.

109   Overall, 3D-STORM imaging and probabilistic modeling provide new insights into SC

110   ultrastructure and reveal a marked reorganization of SC components during meiotic progression

111   (Fig. S2c).

112   **Crossover formation is accompanied by a change in synaptonemal complex organization**

113   Programmed double-strand breaks (DSBs) are generated during early prophase. A subset

114   eventually gives rise to crossover (CO) recombination events. In *C. elegans* each pair of

115   homologous chromosomes undergoes only a single CO, while all other breaks are repaired to

116   yield noncrossover products. Some of the key signaling molecules that regulate CO site selection

4

117   localize to the SC [3, 11-13, 33, 34], and the integrity of this structure is important for CO

118   regulation [9]. Previous work from our group revealed that the SC behaves as a liquid crystal[3],

119   suggesting that diffusing signals and/or structural transitions could be propagated through this

120   material [35]. Interestingly, recent evidence suggests that the central region of the SC grows in

121   length and/or thickness throughout the pachytene stage of meiotic prophase, and that SC proteins

122   may become more stably associated with this structure upon crossover formation [4-7, 9]. Thus,

123   we wondered whether the dramatic reorganization of the SC during meiotic prophase might be

124   linked to crossover formation and might provide a structural basis for the SC's role in CO

125   regulation. We therefore first asked whether the timing of SC reorganization coincides with CO

126   designation. In *C. elegans*, designated crossovers can be visualized as bright GFP-COSA-1 foci,

127   which are first detected in mid-pachytene [36] (Fig. 1a). To test whether the structural transition

128   within the SC coincides with the appearance of bright GFP-COSA-1 foci, we imaged nuclei at

129   mid-pachytene within intact gonads. We inferred the crossover designation status of individual

130   nuclei based on the detection of bright COSA-1 foci and classified them as either mid(-)

131   pachytene or mid(+) pachytene. Throughout mid-pachytene, SYP-1 retains its transverse

132   orientation and both N- and C-termini of SYP-1 are widely distributed in *z* (Fig. 1f,g,m and

133   Table S1). This is consistent with a lateral stacking of SYP-1 molecules in parallel orientation, as

134   observed in early pachytene (Fig. 2a,b). However, the distance of the C-termini of SYP-1 from

135   the central axis of the SC in frontal view was drastically lower in mid(+) pachytene nuclei

136   compared to SCs in mid(-) pachytene nuclei.

137   This indicates that the designation of COs coincides with a conformational switch within

138   the SC. To take an unbiased approach to analyze the dynamics of SC organization during meiotic

139   prophase, we employed principal component analysis (PCA) of SYP-1 and SYP-2 distributions

140   (see methods). The first dimension in the PCA, indicative of the main changes within the SC

141   across different stages during meiotic prophase, corresponds to the transition from early to late

142   pachytene SCs (Fig. 2c). Mid(+) pachytene SCs are similar to late pachytene SCs along the first

143   principal component, while mid(-) SCs are in between early and late pachytene SCs, indicating

144   that the SC is reorganized upon CO designation.

145   In *C. elegans*, designation of COs triggers the asymmetrical remodeling of chromosome

146   axes and the SC to create two domains on either side, known as the long and the short arm.

147   Downstream steps in this differentiation require the recruitment of the Polo-like kinase PLK-2 to

        5

148   the SC [5, 37, 38]. To assess whether the changes we observe in SC ultrastructure are dependent

149   on crossover designation and/or the subsequent remodeling processes, we determined the

150   organization of the SC in *zhp-3(jf61)* null mutants, which lack crossovers [39], and in *plk-*

151   *2(ok1936)* null mutants, which are proficient for CO designation but show pronounced delays in

152   downstream remodeling and arm differentiation [5, 7, 37, 40], although they do eventually

153   segregate most chromosomes properly [38]. We found that SCs in late pachytene in *zhp-3(jf61)*

154   mutants resembled those in early pachytene nuclei in wild-type hermaphrodites, while SCs at late

155   pachytene in *plk-2(ok1936)* mutants are very similar to wild-type (Fig. 1h,i,n, 2 and Fig. S3c,e).

156   Thus, structural reorganization of the SC requires CO designation but is independent of PLK-2.

157   We note that PLK-2 also plays an early role in homologous paring and synapsis [37, 40], and our

158   super-resolution images reveal severe defects in SC architecture in *plk-2(ok1936)* null mutants

159   despite the overall similarity to wild-type late pachytene SCs (Fig. 1i, n). Similarly, while the

160   global SC architecture in *zhp-3(jf61)* mutants resembled early pachytene SCs in wild type, the

161   SC increased in thickness along the optical axis during pachytene in *zhp-3(jf61)* oocytes, based

162   on the spatial distribution of SYP-1 (Fig. 1h, n), consistent with the continuous incorporation of

163   SC subunits even in the absence of crossover formation [5]. In summary, our data indicate that

164   the SC grows in thickness from early to late pachytene independent of crossovers, while the

165   reorganization of SC ultrastructure requires and coincides with CO designation.

166

167   **Defects in SC organization are linked to defects in crossover interference**

168   The SC plays a critical role in regulating the number and distribution of CO

169   recombination events [3, 8, 9, 12, 13]. We therefore wondered whether reorganization of the SC

170   is linked to CO regulation. Fortuitously, in our efforts to isolate a functional C-terminally tagged

171   *syp-4* allele, we identified an unusual, partially functional allele, *syp-4(ie25)* (Fig. 3a). In *syp-*

172   *4(ie25)* homozygotes, we observed timely homologous synapsis, as determined by the length of

173   the transition zone, which corresponds to the leptotene and zygotene stages of meiosis. Six

174   bivalents were consistently observed at diakinesis, indicative of CO formation on all six

175   chromosome pairs (Fig. 3b, c, e). However, super-resolution microscopy indicated that the

176   architecture of the SC was drastically altered in *syp-4(ie25)* late pachytene after crossover

177   formation (Fig. 1l and 2, Extended Fig. S3). SYP-1 lies in a highly tilted orientation (Fig. 2a,b)

178   and the overall conformation of the SC in *syp-4(ie25)* at late pachytene is clearly distinct from

    6

179   any conformation in wild-type animals in our principal component analysis (Fig. 2c). In contrast,

180   early pachytene SCs in *syp-4(ie25)* are more reminiscent of SC conformation of prior to CO

181   formation in wild-type animals (Fig. 1k and 2). These data suggest a strong defect in SC

182   organization in *syp-4(ie25)* that is exacerbated upon CO designation (Fig. 2c).

183   Notably, *syp-4(ie25)* mutant hermaphrodites exhibited high frequencies of chromosome

184   missegregation, resulting in embryonic lethality (38±4% survival, compared to 104% in wild-

185   type) and male self-progeny (6±1% compared to 0.1% in wild-type, Table S2), albeit less severe

186   than in a *syp-4(tm2713)* deletion allele (2.5% viability and 40% males) [18]. Importantly,

187   crossover formation was severely impacted in *syp-4(ie25)*: We observed a slight delay in meiotic

188   progression, indicated by a modest extension of CHK-2 kinase activity [41] (Fig. 3d) and an

189   accumulation of RAD-51 foci, which mark unrepaired recombination intermediates (Extended

190   Data Fig. S4). Moreover, the structure of bivalents at diakinesis was altered in *syp-4(ie25)*

191   oocytes (Fig. 3f), indicating that crossover formation might be affected [42, 43].

192   To better characterize the effects of *syp-4(ie25),* we imaged GFP-COSA-1 to quantify

193   designated crossover sites at late pachynema [36]. Wild-type animals display a single bright

194   GFP-COSA-1 focus on each of the 6 chromosome pairs, even when the number of DSBs is

195   markedly increased [36, 42]. In contrast to the 6±0.2 (s.d.) GFP-COSA-1 foci we observed in

196   wild-type and heterozygous *ie25/+* animals, we observed 10.9±1.7 GFP-COSA-1 foci at late

197   pachytene in homozygous *syp-4(ie25)* hermaphrodites (Fig. 3g, h). This suggested that crossover

198   interference, which in wild-type animals acts over distances longer than any single chromosome

199   [9, 42], is greatly decreased in *syp-4(ie25)* homozygotes. To test this hypothesis, we use two

200   different metrics to quantify the crossover interference strength, the gamma factor [44] and the

201   coefficient of coincidence [45]. Each of these approaches confirmed that crossover interference

202   is severely reduced or absent in *syp-4(ie25)* mutants (Fig. 3i,j).

203   To verify that GFP-COSA-1 foci indeed correspond to designated crossover sites in wild-

204   type and *syp-4(ie25)* animals, we also measured crossing-over genetically using whole genome

205   sequencing (see methods). This confirmed that crossovers in *syp-4(ie25)* homozygotes match the

206   number of GFP-COSA-1 foci. Thus, *syp-4(ie25)* mutants are proficient for synapsis, yet they

207   exhibit drastic alterations in SC architecture and cannot impose normal crossover interference.

208   Crossover interference acts along the physical length of the synapsed chromosomes, and

209   in some organisms chromosomes with longer axes undergo more crossovers than chromosomes

7

210   with shorter axes [46-49]. Therefore, we next asked whether the axis length is increased in *syp-*

211   *4(ie25)* mutants. Interestingly, axes in *syp-4(ie25)* mutants are shorter than in wild-type animals.

212   Thus, changes in axis length cannot account for the observed increase in COs in *syp-4(ie25)*

213   mutants. We hypothesize that the increase in CO number may be caused by the defects in SC

214   organization in *syp-4(ie25)* mutants.

215   Partial depletion of SC proteins in *C. elegans* by RNAi can result in a slight increase in

216   the number of crossovers, to about 7 GFP-COSA-1 foci per nucleus [9]. Thus, we tested whether

217   the defect in crossover regulation in *syp-4(ie25)* can be attributed to reduced levels of SC

218   proteins. The abundance of an epitope-tagged HA-SYP-1 was not altered by the *syp-4(ie25)*

219   mutation (Fig. S5a). However, the immunofluorescence signal of SYP-1 and SYP-2 was reduced

220   in *syp-4(ie25),* although staining appeared contiguous along the chromosomes (Fig. S5b, c). This

221   indicates the *syp-4(ie25)* mutation impairs assembly of SYP proteins between chromosomes. In

222   contrast, we also isolated a mutant, *syp-4(ie27)* (Fig. S6a), which reduced expression levels of

223   SYP-4-HA to about 30% of wild-type (Fig. S6c). Both the transition zone and CHK-2 active

224   zone were extended in *syp-4(ie27)* single mutants, indicating that completion of synapsis and CO

225   designation were delayed (Fig. 3c-d, Fig. S6b, d). We also observed a slight increase in the

226   number of GFP-COSA-1 foci to 7±1.1 (Fig. S6e, Fig. 3g), which is comparable to results

227   obtained for partial depletion of SYP-1, -2 or -3 by RNAi [9], but distinct from our results for

228   *syp-4(ie25)*. This indicates that the defects in crossover interference in *syp-4(ie25)* are not a mere

229   consequence of reduced protein expression.

230   To test whether the defects in SC ultrastructure can account for the effects of *syp-4(ie25)*

231   on crossover regulation, we investigated the role of *syp-4(ie25)* in the regulation of COSA-1 foci

232   within aggregates of SC proteins known as polycomplexes. These bodies self-assemble prior to

233   or after synapsis in many organisms, including in early meiotic nuclei in *C. elegans*. Large

234   polycomplexes also assemble in meiotic nuclei in worms lacking the axis protein HTP-3, and

235   show periodic striations in orthogonal directions that correspond precisely to the width and

236   longitudinal banding of the SC [3, 50]. Intriguingly, we have found that polycomplexes in *htp-3*

237   null mutants recapitulate key aspects of the spatial patterning of CO proteins normally seen along

238   SCs, although these mutant animals lack DSBs and meiotic recombination intermediates.

239   Specifically, at late pachytene, most polycomplexes display a single COSA-1 focus (1.1±0.2;

240   Fig. 4a, b) [3]. When we combined the *syp-4(ie27)* mutation, which reduces expression of SYP-

8

241   4, with Δ*htp-3*, this resulted in smaller polycomplexes, but they showed an identical number of

242   GFP-COSA-1 foci at late pachytene (1.1±0.2) (Fig. 4a, b). By contrast, when *syp-4(ie25)* was

243   combined with Δ*htp-3,* multiple GFP-COSA-1 foci (2.1±0.8) were associated with each

244   polycomplex (Fig. 4a, b), mirroring the ~2-fold increase in GFP-COSA-1 foci observed along

245   bona fide SCs in *syp-4(ie25)* mutants.

246   We thus interrogated the organization of polycomplexes in *syp-4(ie25)* by EM. While

247   structures resembling the electron-dark lateral and brighter, striated central regions were

248   observed in *Δhtp-3 syp-4(ie25)*, the overall organization was dramatically altered: polycomplexes

249   appeared to be internally fragmented, rather than maintaining constant orientation over hundreds

250   of nm, as in "normal" polycomplexes [3] (Fig. 4c), and the distance between parallel electron-

251   dark bands was much narrower (46.3±1.2 nm, vs 97.6±1.5 nm in *Δhtp-3* polycomplexes, Fig.

252   4c), This likely reflects differences in organization and/or orientation of SYP proteins within

253   polycomplexes. Overall, the disorganized structure of polycomplexes in *Δhtp-3 syp-4(ie25)* in

254   EM is reminiscent of the architecture of SCs in *syp-4(ie25)* determined by 3D-STORM. These

255   findings indicate that structural defects within polycomplexes are sufficient to alter special

256   patterning of CO proteins, analogous to the structurally altered SCs that assemble in *syp-4(ie25)*

257   mutants.

258

259   **Discussion**

260   Together these findings establish that the correct organization of the synaptonemal

261   complex is required for spatial patterning of crossovers, and further corroborate previous

262   findings that the SC is important for crossover interference. They further suggest that CO

263   regulation may involve transduction of structural information through this liquid crystalline

264   material. This idea is reminiscent of a "beam-film" model for crossover interference, which

265   proposes that crossovers relieve local stress along a beam-like material [49, 51]. This mechanical

266   stress has been proposed to be imposed by chromatin structure and/or tethering of chromosomes;

267   however, our findings reinforce previous studies that implicated the SC as a crucial mediator of

268   crossover patterning [8, 9, 12]. In particular, we have reported that polycomplexes comprised of

269   SC central region proteins alone can mediate spatial patterning of GFP-COSA-1 foci even in the

270   absence of association with chromatin or axis proteins, and polycomplexes in *syp-4(ie25)*

271   mutants exhibit both defects in their internal organization and altered patterning of GFP-COSA-1

9

272   foci. Interestingly, forces applied to nematic liquid crystalline materials such as the SC [3] can

273   perturb the orientation of molecules within the liquid crystal [35]. Therefore, we speculate that

274   the reorganization of proteins within the SC that occurs concomitant with CO designation may

275   reflect a mechanical signaling component of CO interference.

276

277

278   **Figures**
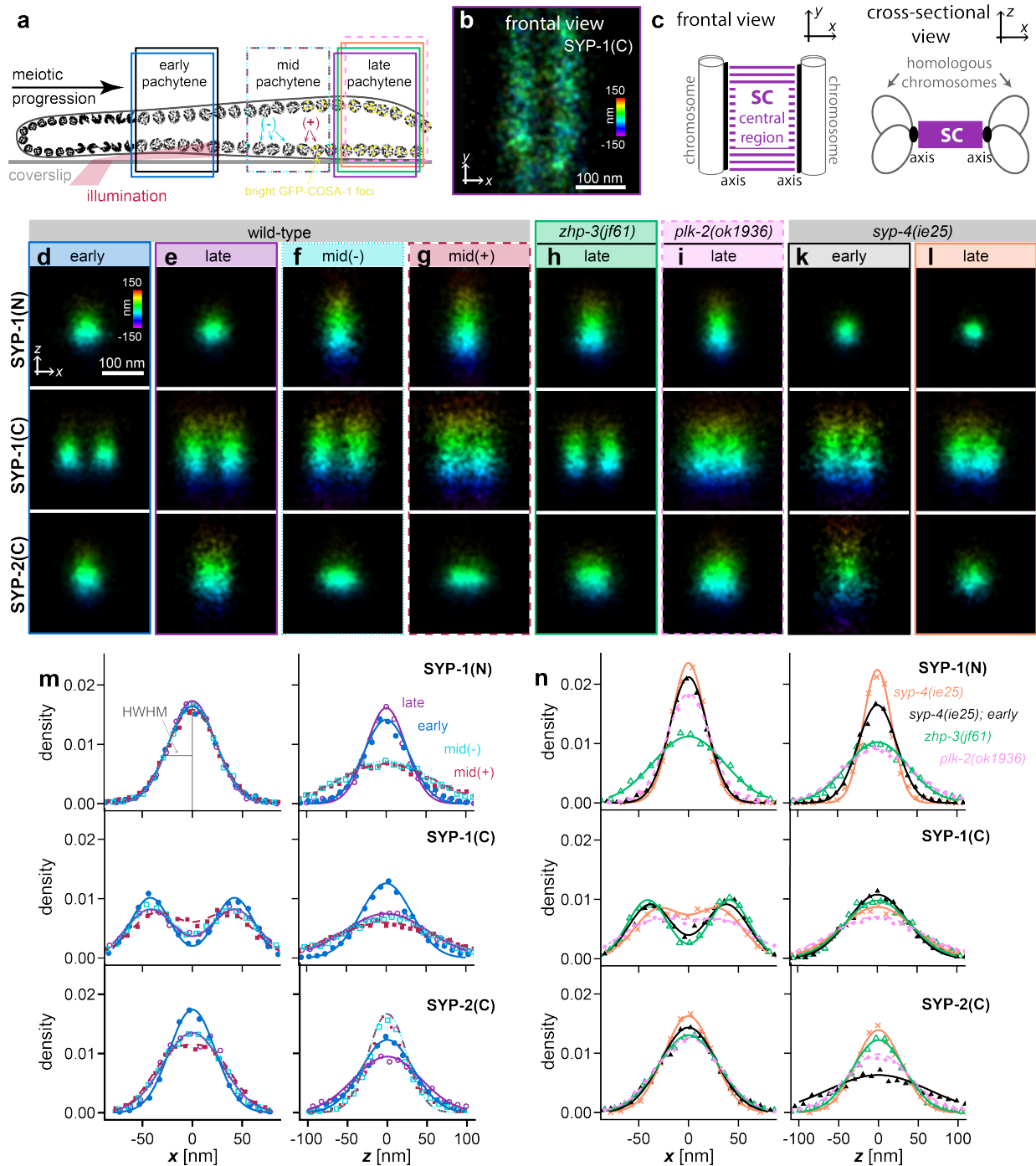
279
280

281   **Figure 1: Super-resolution microscopy reveals the dynamic three-dimensional organization**

282   **of the synaptonemal complex.** (a) In the *C. elegans* gonad, nuclei (representative DAPI images)

283   are arranged in a gradient of premeiotic and meiotic stages. Using highly inclined illumination

11

284   (red), we imaged SCs in the bottom section of nuclei adjacent to the coverslip (gray) in early,

285   mid- and late pachytene (rectangles). Mid(-) (cyan) and mid(+) (red) pachytene correspond to

286   nuclei without and with bright GFP-COSA-1 foci in the same field of view, respectively. (b)

287   Measurements based on averaged STORM images indicate that the C-terminus of SYP-1 lies

288   close to the chromosome axes. Colors denote localizations in z from -150 to 150 nm (color scale

289   bar). (c) The schematic depicts the SC, which forms a ladder-like structure approximately 100-

290   nm wide (purple), which links the axes (black) of paired homologous chromosomes (white rods)

291   in the frontal view (left). To visualize the 3D architecture of the SC, we show cross-sectional

292   views of the SC as depicted (right). (d-l) Averaged cross-sectional views of STORM images for

293   the N-terminus of HA-SYP-1 (top row), the C-terminus of SYP-1 (center row), and C-terminus

294   of SYP-2 (bottom row), for wild-type SCs in early (d, blue closed spheres in m), late (e, purple

295   closed spheres in m), mid(-) (f, cyan open squares in m), and mid(+) (g, red closed squares in m)

296   pachytene and for *zhp-3(jf61)* (h, green triangles, late pachytene in n), *plk-2(ok1936)* (i, pink

297   diamonds in n, late pachytene) and *syp-4(ie25)* (k, black closed triangles for early pachytene

298   orange crosses in late pachytene in n). (m, n) Histograms of localization events in frontal view

299   (x, left) and across the SC (z, right) are fitted with 1 or 2 Gaussians. The results of the fits are

300   summarized in Extended Data Table S1.

12

301

302
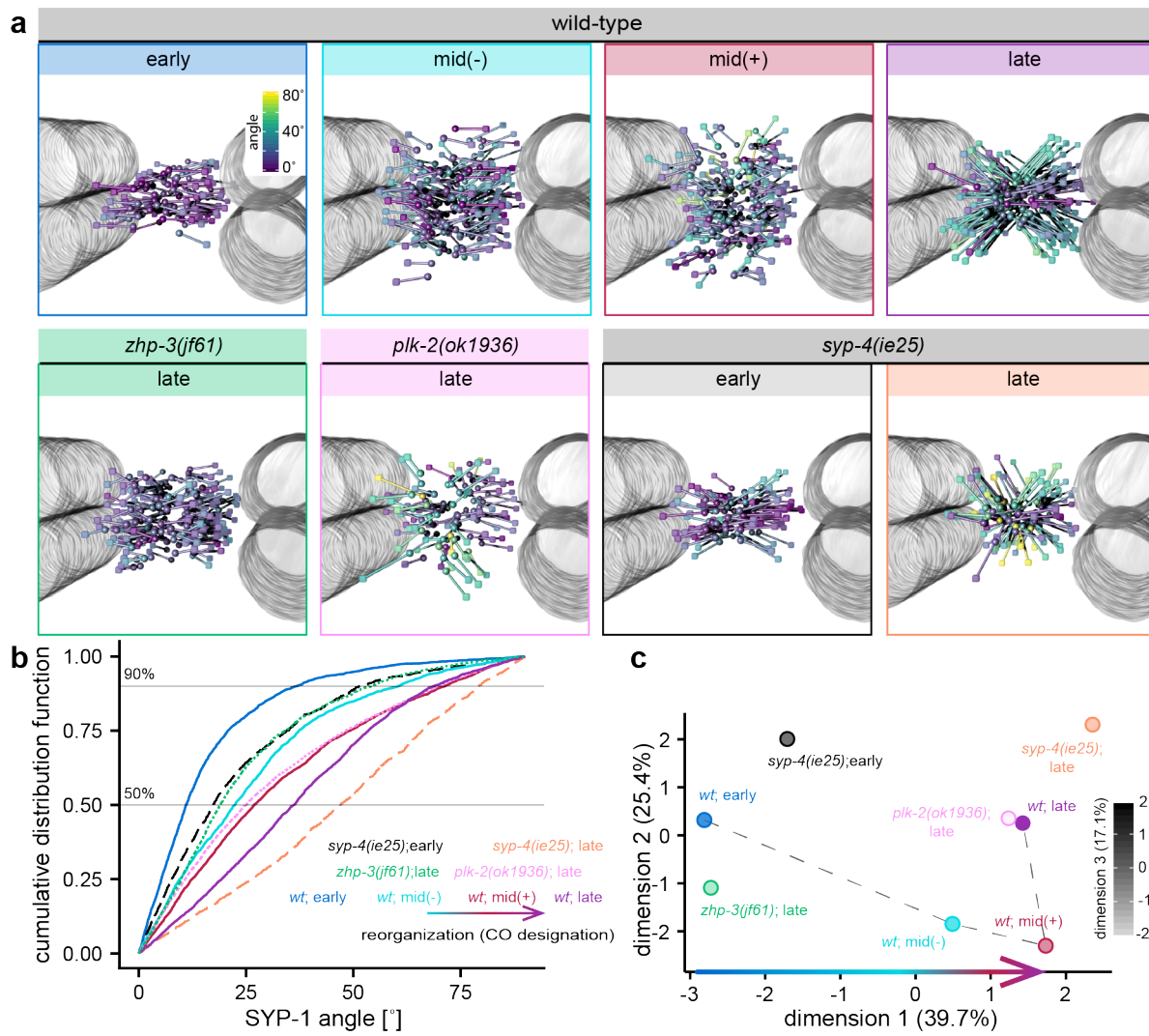
Figure 2: The synaptonemal complex undergoes a structural transition upon crossover designation. (a) The stochastic nature of STORM does not allow us to image the N- and C-terminus of a specific single molecule at the same time but will yield population averages for the localization of individual domains. We therefore used a probabilistic mapping approach to reconstruct the orientation of SYP-1 molecules for each condition and genotype. The resultant models of SYP-1 (black) are shown with C-termini depicted as cubes and N-termini as spheres. A proxy for chromatin (gray areas) is added for visualization purposes. Models are rendered using POV-ray (v3.7.0). Models show changes in the orientation of SYP-1 upon crossover formation. (b) These changes are revealed by the distributions of angles of SYP-1 with respect to the central plane of the SC in cross-sectional views. Cumulative distribution functions are shown. Gray horizontal lines mark median (50%) and 90th percentile values. (c) A principal component analysis (see methods) summarizes the SC organization at different conditions and

13

315   genotypes. The progression of SC reorganization in wild-type animals throughout pachytene is
316   highlighted by a gray dashed line. Dimension 1 scales with SC reorganization upon crossover
317   formation (colored arrow). We note that mid(-) SCs prior to designation of COs marked by
318   bright GFP-COSA-1 foci are closer to late pachytene than early pachytene. This suggests that
319   some aspects of the transition in SC reorganization may occur even prior to the appearance of
320   GFP-COSA-1 foci and/or nuclei designated mid(-) pachytene may include false negatives given
321   that our field of view in *z* is limited to 1 µm slices and does not contain whole nuclei. SC
322   organization in late pachytene *zhp-3(jf61)* mutants that lack CO formation is similar to wild-type
323   early pachytene, while SCs in *plk-2(ok1936)* null mutants resemble wild-type SCs. By contrast,
324   SCs in *syp-4(ie25)* mutants are distinct in both early and late pachytene.

14
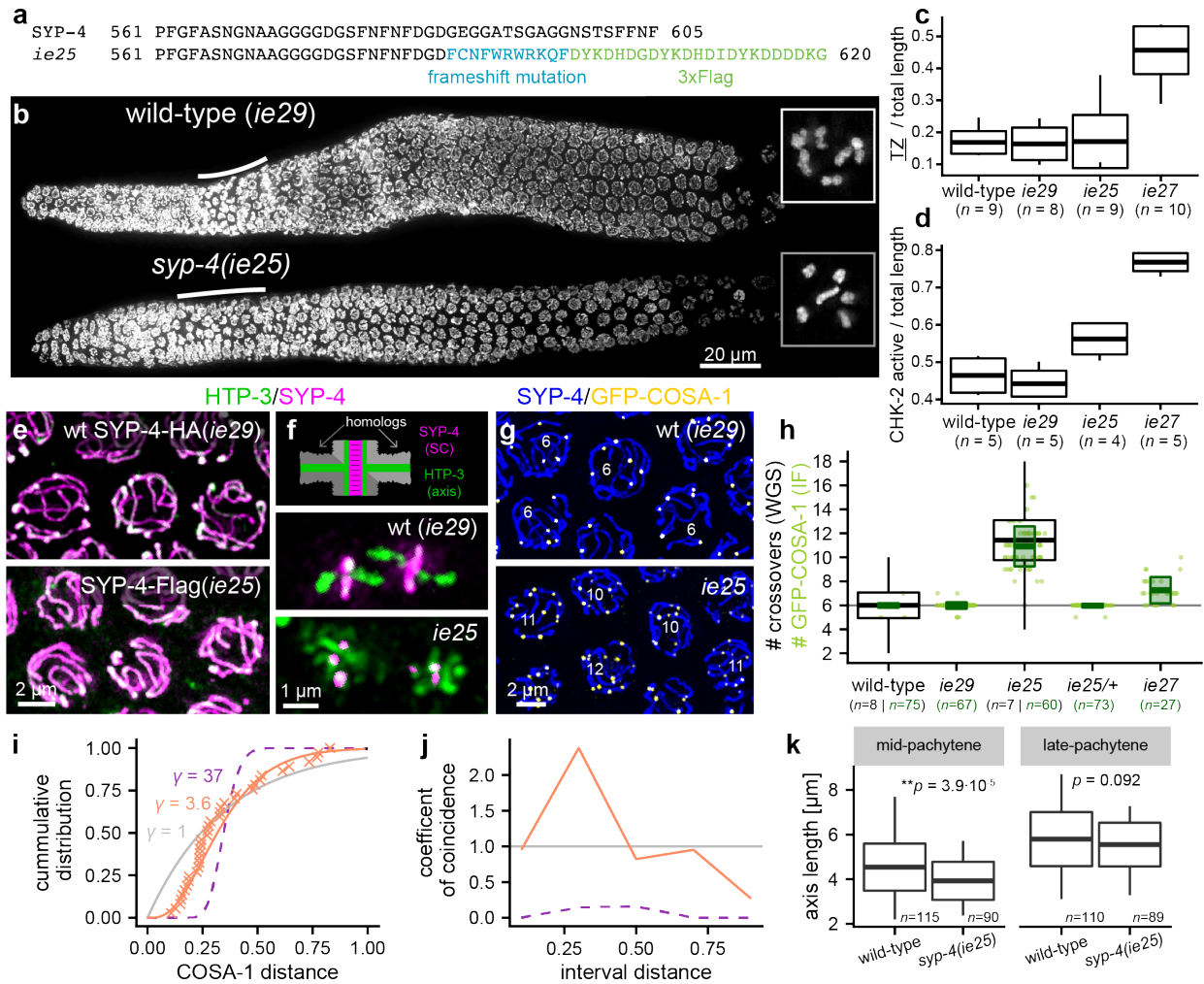
Figure 3: Crossover interference is diminished in *syp-4(ie25)* mutants. (a) The C-terminal amino-acid sequences of wild-type SYP-4 and SYP-4(*ie25*) are indicated. (b) Fluorescence micrographs of DAPI-stained gonads from wild-type (*syp-4-ha(ie29)*, top) and *syp-4(ie25)* mutants (bottom). Insets depict single oocyte nuclei, revealing 6 bivalents in both wild-type and *syp-4(ie25)*. (c) The *syp-4(ie25)* mutation or epitope tagging of *syp-4* alone *(ie29)* did not perturb the length of the transition zone (solid lines in b), but this length was significantly increased in *syp-4-ha(ie27)* mutants, indicative of a defect in synapsis. (d) Immunofluorescence detection of a CHK-2-dependent phoshpoepitope provides a more consistent assay for meiotic progression. In animals homozygous for the syp-4-HA allele *ie29,* this "CHK-2 active" zone comprises 45% of the length of the germline containing leptotene, zygotene and pachytene stages of meiosis. This fraction was extended to 56% and 77% in *ie25* and *ie27*, respectively. Boxplots in c and d show mean±s.d (whiskers show minima and maxima). (e) Fluorescence micrographs reveal robust synapsis for *ie29* (top) and *ie25* (bottom). (f) The cruciform bivalent structure, as illustrated in the cartoon (top) is disrupted in *ie25*, likely reflecting the occurrence of multiple crossovers per

15

341   chromosome pair. Immunostaining of HTP-3 (axis; green) and SYP-4 (SC; magenta) is shown

342   (e-f). (g) The number of crossovers per nucleus as estimated from whole genome sequencing

343   (black/white boxplots, mean±s.e., whiskers are extreme values) correspond to the number of

344   GFP-COSA-1 foci (green dots and boxplots, mean±s.d.). (h) Fluorescence micrographs show a

345   marker for designated crossovers, GFP-COSA-1 (yellow), and SYP-4 (blue). (i) To measure

346   crossover interference strength, we fit the cumulative distribution function of inter-GFP-COSA-1

347   distances in *syp-4(ie25)* mutants (orange crosses) using a gamma function[44]. $\gamma=1$ denotes no

348   interference (gray), $\gamma=37$ corresponds to interference measured for wild-type animals[9] (purple

349   dashed line), while interference in *syp-4(ie25)* is severely reduced to $\gamma=3.5$ (orange line, $n=41$

350   chromosomes). (j) Likewise, interference strength can be described by the coefficient of

351   coincidence[45], which denotes the ratio of the observed number of 2 COs (GFP-COSA-1 foci)

352   at a given distance to the expected number assuming random CO distribution. In wild-type

353   animals, the coefficient of coincidence of GFP-COSA-1 foci is 0 corresponding to complete

354   interference (purple dashed line; $n=88$ chromosomes), while it is approximately 1 in *syp-4(ie25)*

355   mutants (orange, $n=41$), indicating no interference (gray line). (k) Chromosome axes lengths are

356   shorter in *syp-4(ie25)* mutants compared to wild-type axes in mid(-)-pachytene prior do

357   designation of CO sites (left) and comparable in late pachytene (right). Boxplots show mean±s.d

358   and whiskers are extreme values.

359

360

361

16

362
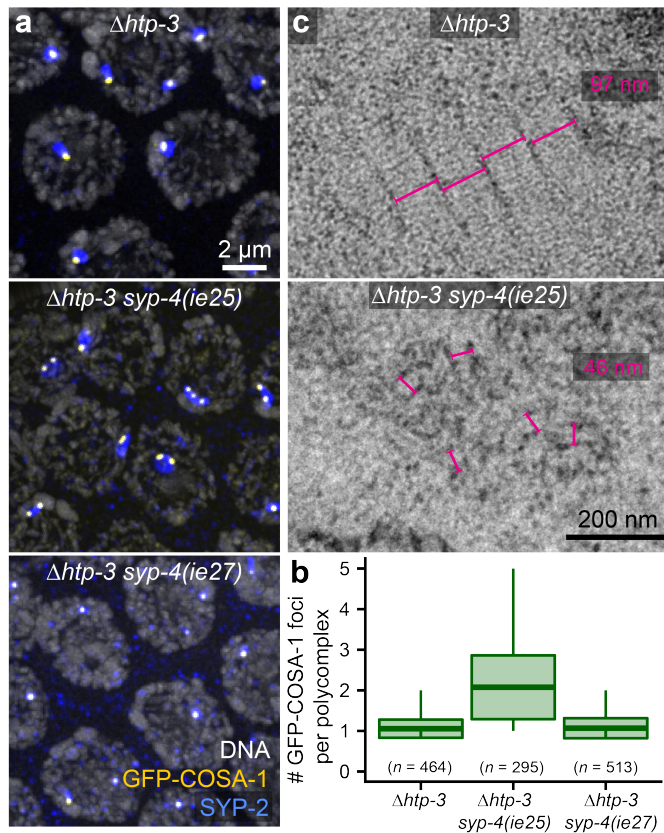
363

364 **Figure 4: Irregular organization and an increase in GFP-COSA-1 foci in** *syp-4(ie25)*

365 **polycomplexes.** (a) Fluorescence micrographs show that the number of GFP-COSA-1 foci

366 (yellow) is limited to 1 or 2 per polycomplex (SYP-2, blue) in wild-type conditions (Δ*htp-3*) and

367 in the presence of *syp-4(ie27)* but is elevated in *syp-4(ie25)*. DAPI is shown in gray. (b)

368 Quantification of GFP-COSA-1 foci. Boxplots show mean±s.d. and whiskers are extreme values.

369 (c) Representative electron micrographs show that the SC-like structure of polycomplexes (Δ*htp-*

370 *3*, 97 nm spacing of parallel, electron dark regions) is disturbed in Δ*htp-3 syp-4(ie25)*, which are

371 disorganized and 46 nm apart.

372

373

374

17

375 **Table S1: Summary of localizations of SC components determined by STORM.** Positions

376 are distances of the maxima to the center of the SC (wt = wild-type; early = early pachytene;

377 mid(-) = mid pachytene nuclei without bright GFP-COSA-1 foci; mid(+) = mid pachytene nuclei

378 with bright GFP-COSA-1 foci). HWHM denotes the half width at half maximum of the

379 distributions (Fig. 1m, gray lines)

domain	condition	x [nm] position	x [nm] HWHM	z [nm] position	z [nm] HWHM	total length analyzed [nm] (# images)
HA-SYP-1	wt, early	0	28.3 ± 1.8	0	33.1 ± 2.7	3438 (8)
	wt; mid(-)	0	27.5 ± 1.6	0	65.4 ± 2.8	3056 (5)
	wt; mid(+)	0	29.4 ± 2.6	0	69.7 ± 3.5	3992 (6)
	wt, late pachytene	0	27.0 ± 1.6	0	29.1 ± 3.7	4780 (9)
	zhp-3(jf61)	0	42.7 ± 2.5	0	46.9 ± 2.9	3579 (7)
	plk-2(ok1936)	0	25.5 ± 1.5	0	52.0 ± 3.9	4136 (10)
	syp-4(ie25); early	0	22.1 ± 1.4	0	28.6 ± 1.2	4351 (10)
	syp-4(ie25); late	0	19.8 ± 0.8	0	20.5 ± 1.6	3114 (6)
SYP-1(C)	wt, early	42.3 ± 0.8	22.8 ± 0.9	0	37.1 ± 2.3	4092 (7)
	wt; mid(-)	40.8 ± 1.3	28.2 ± 0.6	0	68.1 ± 4.3	3184 (7)
	wt; mid(+)	35.9 ± 0.9	31.2 ± 1.0	0	78.7 ± 2.8	3503 (7)
	wt, late pachytene	42.0 ± 1.2	28.5 ± 1.0	0	62.7 ± 3.2	5312 (9)
	zhp-3(jf61); late	41.0 ± 1.3	23.6 ± 1.1	0	48.2 ± 4.3	1851 (8)
	plk-2(ok1936); late	36.3 ± 1.4	39.6 ± 3.6	0	67.0 ± 2.5	5741 (9)
	syp-4(ie25);	38.5 ± 2.5	24.9 ± 0.8	0	43.2 ± 3.8	2768 (5)

18

	early					
	syp-4(ie25); late	30.5 ± 1.5	29.1 ± 1.8	0	54.0 ± 2.2	4848 (6)
SYP-2(C)	wt, early	0	27.0 ± 2.0	0	38.3 ± 3.7	5866 (10)
	wt; mid(-)	16.3 ± 7.5	27.1 ± 2.7	0	27.6 ± 1.1	8437 (9)
	wt; mid(+)	20.6 ± 6.3	26.5 ± 3.6	0	27.7 ± 1.4	8615 (12)
	wt, late pachytene	18.9 ± 2.1	21.6 ± 1.5	0	49.5 ± 5.0	4573 (9)
	wt, late (HA)	20.9 ± 0.9	20.0 ± 1.3	0	39.9 ± 2.6	2958 (8)
	zhp-3(jf61); late	0	36.1 ± 4.3	0	38.6 ± 3.8	3746 (6)
	plk-2(ok1936); late	0	37.1 ± 2.0	0	47.4 ± 2.3	8206 (9)
	syp-4(ie25); early	0	32.4 ± 2.2	0	73.6 ± 8.8	3172 (7)
	syp-4(ie25); late	0	28.9 ± 2.7	0	33.4 ± 3.2	3604 (8)
GFP-SYP-3	wt, early	0	23.3 ± 0.8	0	40.0 ± 4.5	1784 (4)
	wt, late pachytene	0	18.5 ± 1.4	0	63.2 ± 6.2	2238 (6)
SYP-3-HA	wt, early	12.3 ± 1.8	20.3 ± 1.2	0	27.1 ± 2.4	4653 (10)
	wt, late pachytene	16.6 ± 4.7	29.0 ± 2.3	0	48.1 ± 5.9	2764 (7)
	zhp-3(jf61); late	14.2 ± 2.0	24.4 ± 1.4	0	28.5 ± 2.2	2723 (6)
SYP-4-intFlag	wt, early	0	25.8 ± 0.9	0	43.3 ± 5.3	3462 (9)
	wt, late pachytene	0	30.3 ± 4.3	0	49.8 ± 4.6	2524 (4)
SYP-4-HA	wt, early	14.2 ± 2.0	23.0 ± 1.6	0	38.6 ± 2.4	5355 (10)

19

	wt, late pachytene	0	36.8 ± 1.1	33.1 ± 11.9	51.5 ± 8.0	5264 (9)
SYP-4(*ie25*)	syp-4(ie25); late	0	29.1 ± 1.1	0	54.9 ± 5.6	4611 (9)
HIM-3	wt, early	33.5 ± 5.2	43.4 ± 2.3	n.d.	n.d.	2548 (6)
	wt, mid(-)	41.4 ± 2.2	46.7 ± 1.8	n.d.	n.d.	3661 (7)
	wt, mid(+)	41.8 ± 1.9	45.1 ± 1.2	n.d.	n.d.	2817 (7)
	wt, late pachytene	47.3 ± 1.5	30.2 ± 1.2	n.d.	n.d.	4411 (11)
	zhp-3(jf61); late	45.9 ± 1.6	49.0 ± 2.3	n.d.	n.d.	6969 (11)
	plk-2(ok1936); late	41.5 ± 3.8	53.9 ± 4.1	n.d.	n.d.	4769 (8)
	syp-4(ie25); early	45.3 ± 3.6	48.9 ± 2.7	n.d.	n.d.	3900 (7)
	syp-4(ie25); late	35.8 ± 3.8	45.9 ± 3.1	n.d.	n.d.	2926 (6)

380

381
382
383
384

385 **Table S2: List of Strains used in this study and their characterization.** *p*-Values for deviation

386 from wild-type are calculated using Mann-Whitney tests.

387

name	genotype	egg viability [%] (*p*-value)	males [%] (*p*-value)	# of eggs
N2	*wild-type*	104±6	0.08±0.20	4773
GFP-COSA-1 [36]	*meIs8* II	107±4	0.00±0.00	1362
mEos-HIM-3 [24]	*meIs8* II; *him-3(ie33)* IV	n.d.	n.d.	
mMaple-HIM-3 [24]	*meIs8* II; *him-3(ie34)* IV	n.d.	n.d.	
HA-SYP-1	*meIs8* II; *him-3(ie33)* IV; *syp-1(ie40[syp-1(1-47)::HA::syp-1(48-489)])* V	100±4 (0.886)	0.00±0.00 (0.452)	840
SYP-2-HA	*meIs8* II; *him-3(ie33)* IV; *syp-2(ie99[syp-2::HA])* V	101±6 (0.394)	0.00±0.00 (1.00)	1405
GFP-SYP-3	*syp-3(ok758)* I; *ieSi11 [syp-3p::syp-3::EmGFP::syp-3-3'UTR + unc-119(+)]* II; *him-3(ie33)* IV	83±10 (0.031)	0.87±0.59 (0.045)	1143
SYP-3-HA	*syp-3(ie42[syp-3::HA])* I; *meIs8* II; *him-3(ie33)* IV	95±4 (0.041)	1.80±0.60 (0.004)	1457
SYP-4-HA(*ie29*)	*syp-4(ie29[syp-4::HA])* I; *meIs8* II; *him-3(ie34)* IV	100±2 (0.150)	0.72±0.41 (0.052)	1336
SYP-4-HA(*ie29*)	*syp-4(ie29[syp-4::HA])* I; *meIs8* II	105±3 (0.686)	0.00±0.00 (1.000)	951
SYP-4-intFlag	*syp-4(ie30[syp-4(1-315)::2xFlag::syp-4(319-605)])* I; *meIs8* II; *him-3(ie33)* IV	98±3 (0.032)	1.91±0.59 (0.010)	1350
SYP-4(*ie25*)	*syp-4(ie25[syp-4ΔC::3xFlag])* I; *meIs8* II	38±4 (0.008)	5.97±1.25 (0.010)	1024
SYP-4-HA(*ie27*)	*syp-4(ie29[syp-4::HA::mod3'UTR])* I; *meIs8* II	80±9 (0.002)	1.58±1.58 (0.010)	992
Δ*htp-3* [3]	*htp-3(tm3655)* I; *meIs8* II	n.d.	n.d.	
Δ*htp-3 syp-4(ie25)*	*htp-3(ie100) syp-4(ie25)* I; *meIs8* II	n.d.	n.d.	

21

*Δ**htp-3 syp-4(ie27)***	*htp-3(ie101) syp-4(ie27)* I; *meIs8* II	n.d.	n.d.	
SYP-4(*ie25*)	*syp-4(ie25[syp-4ΔC::3xFlag])* I; *meIs8* II; *him-3(ie33)* IV	n.d.	n.d.	
SYP-4(*ie25*); HA-SYP-1	*syp-4(ie25)* I; *meIs8* II; *him-3(ie33)* IV; *syp-1(ie40)* V	n.d.	n.d.	
zhp-3(jf61)	*zhp-3(jf61)* I; *meIs8* II; *him-3(ie33)* IV	n.d.	n.d.	
zhp-3(jf61); **HA-SYP-1**	*zhp-3(jf61)* I; *meIs8* II; *him-3(ie33)* IV; *syp-1(ie40)* V	n.d.	n.d.	
zhp-3(jf61) **SYP-3-HA**	*syp-3(ie102[syp-3::HA]) zhp-3(jf61)* I; *meIs8* II; *him-3(ie33)* IV	n.d.	n.d.	
plk-2(ok1936); **HA-SYP-1**	*plk-2(ok1936)* I; *meIs8* II; *him-3(ie33)* IV; *syp-1(ie40)* V	n.d.	n.d.	

388
389
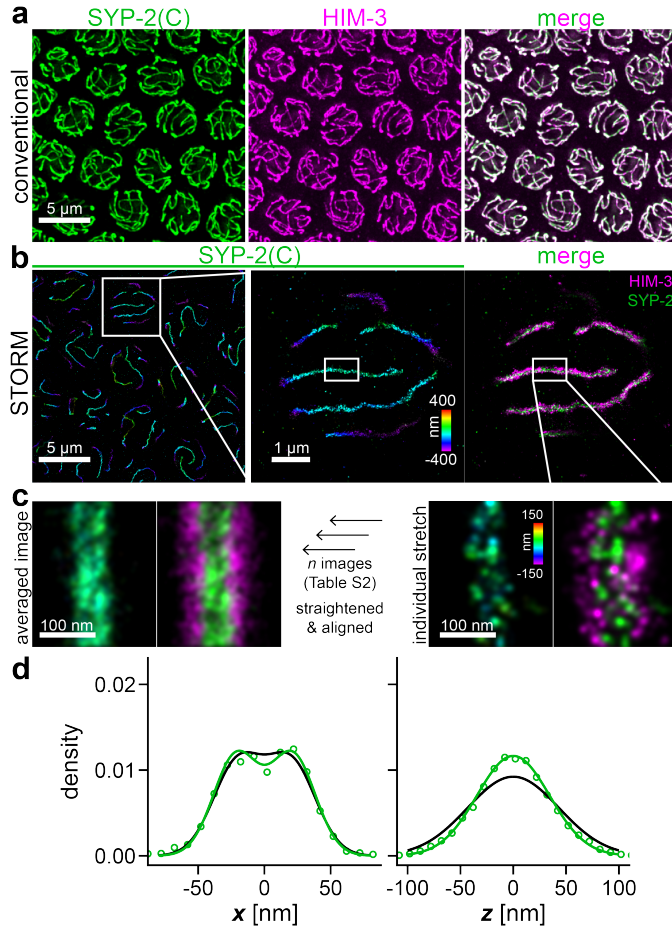
Extended Data Figure S1: Experimental strategy for mapping the architecture of the synaptonemal complex. (a) The resolution in conventional fluorescence micrographs is insufficient to visualize the structure of the axis or SC (HIM-3, magenta, left) and SC components (SYP-2-HA, green, center) are co-localized (merge, right). (b) The structure of the SC is resolved by STORM super-resolution microscopy. Colors denote localization in z (left and center). Localization of HIM-3 (magenta, right) is used to determine the orientation of the SC (SYP-2-HA(C), wild-type, late pachytene in green). White boxes in b show regions magnified in other panels. (c) For further analysis, individual stretches in frontal view (right), which are characterized by clearly separated HIM-3 axes, are straightened and aligned in x and z to generate the averaged image (left). (d) The results are highly reproducible between different preparations and different antibodies (SYP-2(C) peptide antibody, black, and SYP-2-HA epitope antibody, green) (Table S2). Note that the widths of the distributions are narrower for the monoclonal HA antibody compared to the polyclonal SYP-2(C) peptide antibody.

23

405
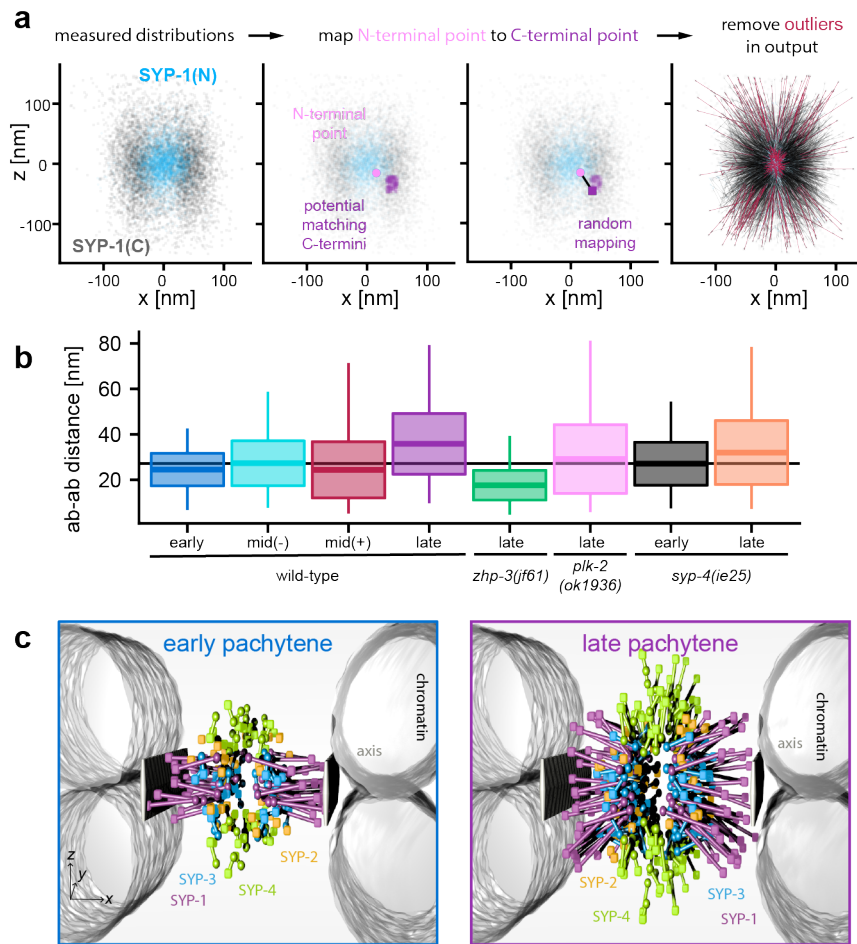
406
407 **Extended Figure S2: Dynamic orientation of SYP-1 molecules.** (a) To generate a model of

408 SYP orientation within the SC, individual datapoints (magenta circle, center) in the measured

409 distributions of the N- (blue, left) and C-terminus (gray, left) of a given component (here: SYP-1

410 in wild-type late pachytene) are randomly mapped to a localization event within the same

411 percentile ±7.5% tolerance of the C-terminal distribution in x and z (purple, center). Mapped

412 events resulting in the shortest or longest 5% of antibody to antibody distances (red, right) are

413 disregarded. (b) The boxplots show means±s.d. of the distances between N- and C-terminal

414 antibodies as estimated by the probabilistic mapping approach. Whiskers are extremes and the

415 black line shows the mean across all genotypes and conditions. (c) The resultant model of SC

416 organization generated by mapping of N- and C-terminal distributions of SYP proteins is shown

417 for early (left) and late (right) pachytene in wild-type animals. C-termini are cubes and N-termini

24

418 (central domain for SYP-4) are spheres. The localization of HIM-3 in x is used as a proxy for

419 axis localization. Models are rendered using POV-ray (v3.7.0).

420

421

25

422
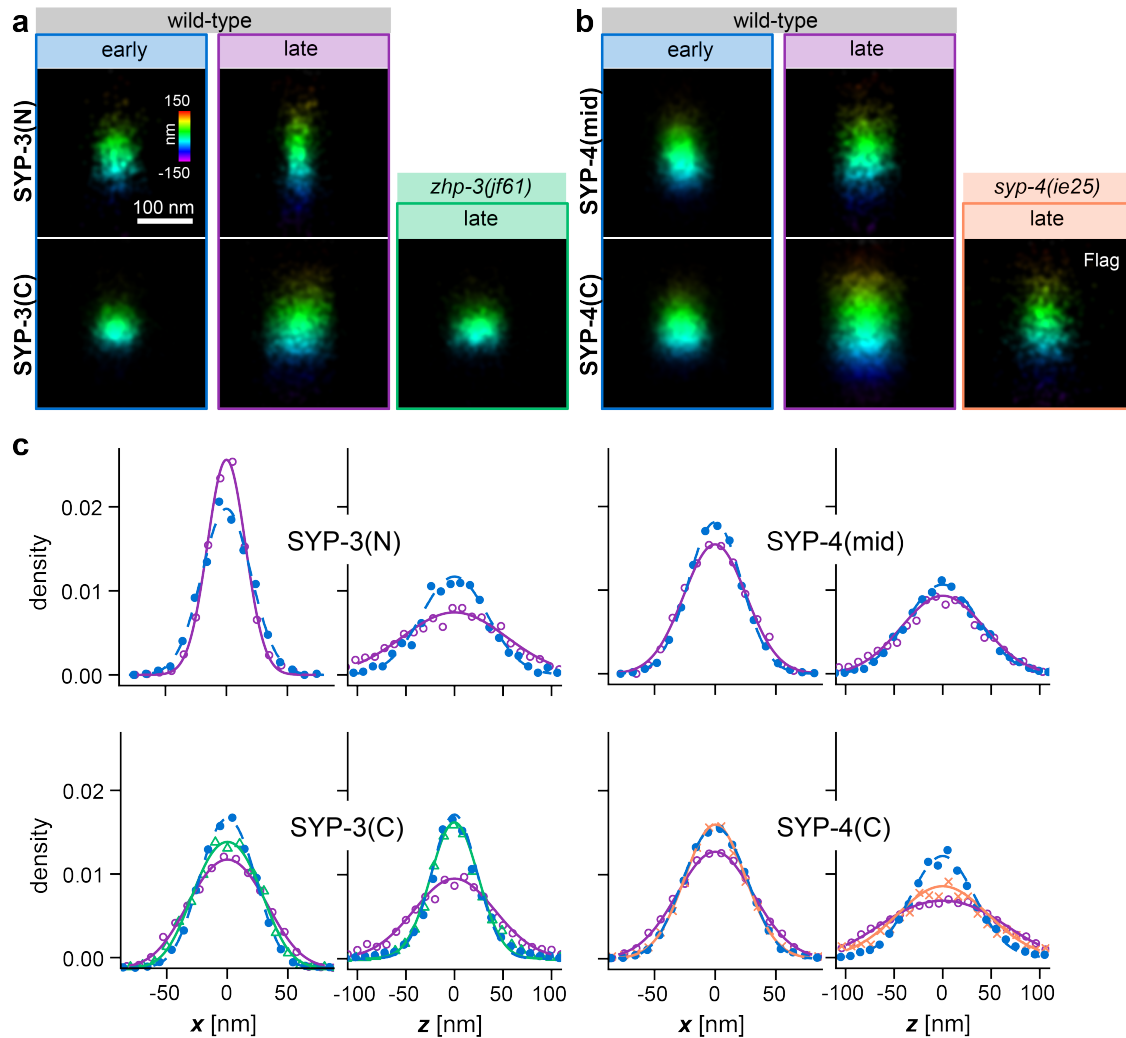
423

424 **Extended Data Figure S3: Dynamic organization of SYP-3 and SYP-4 within the SC.** (a-b)

425 Averaged STORM images show cross-sectional views of SYP-3 (a) and SYP-4 (b) domains as

426 indicated in wild type at early (blue) and late pachytene (purple) and *zhp-3(jf61)* (orange) and

427 *syp-4(ie25)* (green) mutants in late pachytene. Colors denote localization in *z*. The distributions

428 of localization events in frontal (*x*), and vertical (*z*) views are analyzed in (c). The results are

429 summarized in Extended Data Table S2.

430

431

432

26

433
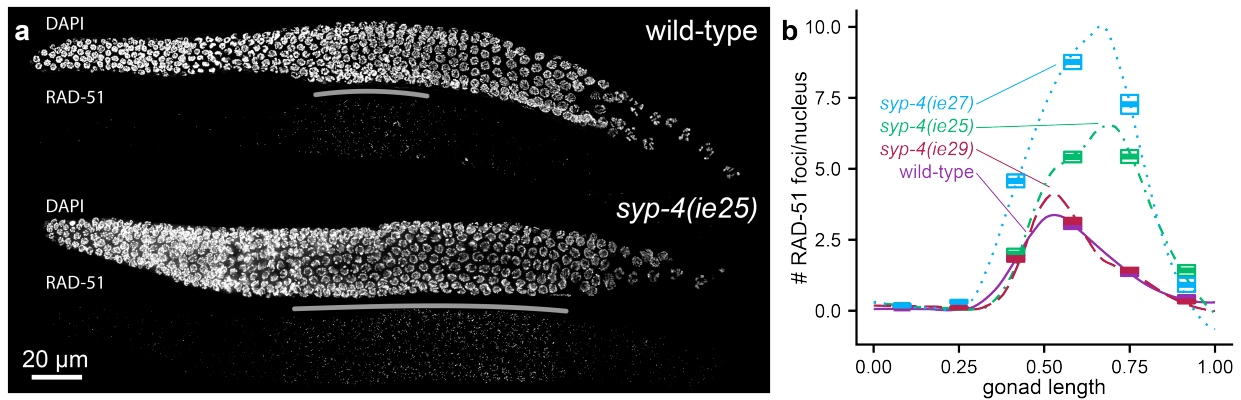
434

435   **Extended Data Figure S4: Double-strand break formation is extended in *syp-4(ie25)*.** (a)

436   Immunofluorescence images show DAPI (upper) and RAD-51 (lower), which marks double-

437   strand breaks. While the RAD-51 zone (gray line) is normally limited to a short region in

438   early/mid-pachytene in wild-type (top), it is markedly elongated in *syp-4(ie25)* (bottom). (b)

439   shows the average number of RAD-51 foci per nucleus (boxes are mean±s.e.) as a function of the

440   relative length of the gonad from the distal tip to the end of pachynema of wild-type (purple solid

441   line, *n*=1672 nuclei from (7) gonads), *syp-4(ie29)* (red dashed line, *n*=1407 (6)), *syp-4(ie25)*

442   (green dot-dashed line, *n*=1440 (6)) and *syp-4(ie27)* (blue dotted line, *n*=1162 (4)), respectively.
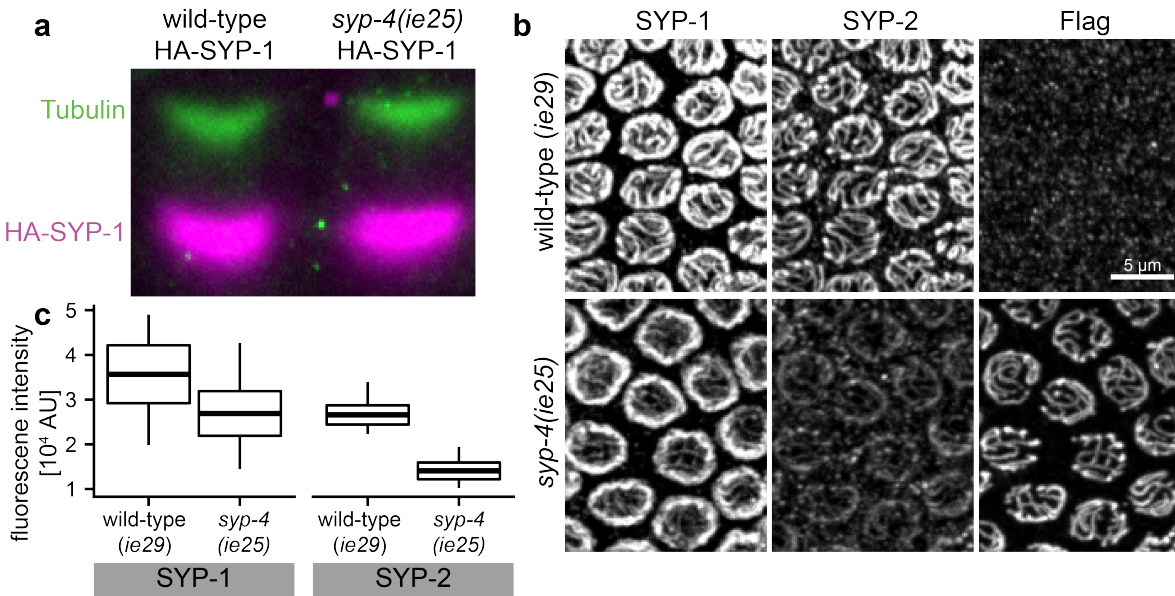
443
444
445
446

27

447

448

449 **Extended Data Figure S5: Abundance of SC proteins in *syp-4(ie25)*.** (a) The expression level

450 of HA-SYP-1 (magenta) is identical in wild-type and *syp-4(ie25)* strains as shown by a Western

451 Blot. Tubulin (green) is shown as a reference. (b) By contrast, the levels of immunofluorescence

452 staining for SYP-1 (left) and SYP-2 (center) are drastically reduced in *syp-4(ie25)* SCs (bottom)

453 compared to wild-type (*syp-4-ha(ie29)*, right). To ensure identical handling, gonads from both

454 genotypes were stained in a single reaction and their genotype was determined by anti-Flag

455 staining (right), which marks *syp-4(ie25)* but not *syp-4(ie29)*. (c) Boxplots show mean±s.d.

456 (whiskers are extreme values) of fluorescence intensities of late pachytene SCs (*ie29*: *n*=339,
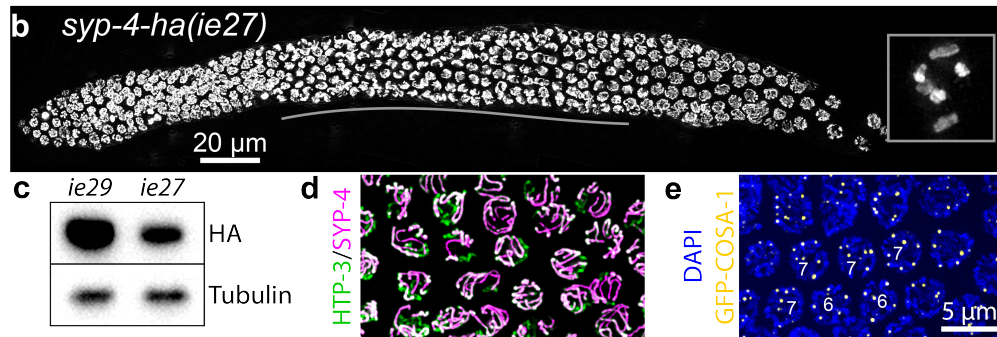
457 *ie25*: *n*=209).

458

459

460

461

28

462

463

464 **Extended Data Figure S6: The *syp-4-ha(ie27)* mutation phenocopies partial RNAi of other**

465 **SC components.** (a) The mutation *syp-4-ha(ie27)* (bottom) is constituted by an insertion (cyan)

466 in the 3' untranslated region (lower case letters) of the *syp-4* gene, but the coding sequence

467 (capital letters) is identical to *syp-4-ha(ie29)* (top), which is phenotypically wild-type. (b) A

468 DAPI stained fluorescence micrographs show that meiotic progression is delayed in *syp-4-*

469 *ha(ie27)* as indicated by an elongated transition zone (gray line) but can form 6 bivalents (inset)

470 indicating largely successful homologous pairing and crossover formation. (c) A western blot

471 shows that the level of SYP-4-HA (top) is reduced to ~ 30 % in *syp-4-ha(ie27)* compared to *syp-*

472 *4-ha(ie29)*. Tubulin is shown as a reference (bottom). (d) Synapsis is delayed in *syp-4-ha(ie27)*

473 as shown by the incomplete overlap of immunofluorescence images of an axial protein (HTP-3,

474 green) and SC proteins (SYP-4-HA, magenta). (e) As has been described for partial RNAi

475 depletion of SYP-1, -2 and -3[9], a reduction in SYP-4 expression level results in a slight

476 increase in the number of GFP-COSA-1 (yellow) foci to about 7 foci/nucleus (DAPI is shown in

477 blue).

478

479

29

Methods

Worm strains and transgenes

A complete list of *C. elegans* strains used in this study can be found in Table S1. All strains were cultured at 20ºC using standard methods[52]. GFP-SYP-3[32] was inserted by MosSCI[53] and crossed into *syp-3(ok758)*. Other tags were inserted using CRISPR-Cas9 genome editing as described in[24]. Briefly, Cas9 and gRNA were delivered by microinjection, either encoded on a plasmid[54] or as *in vitro* preassembled Cas9-ribonucleoprotein complexes. Repair templates for small epitope tags were codon optimized for *C. elegans* [55] and synthesized as "Ultramers" by IDT.

Immunofluorescence

Immunofluorescence of dissected gonads from young adults 24 h post L4 was performed as described[56] with modifications described in[24]. The following primary antibodies, all of which have been previously described, were used: goat anti-SYP-1 (1:500, affinity purified)[37], mouse anti-HA (1:500, monoclonal 2-2.2.14, Thermo Fisher Scientific), rabbit anti-SYP-2 (1:500, affinity purified)[16], mouse anti-GFP (1:500, monoclonal 7.1 and 13.1, Roche), mouse anti-Flag (1:500, monoclonal M2, Sigma-Aldrich), chicken anti-HTP-3 (1:500)[57], rabbit anti-HIM-3 (1:500, SDQ4713 ModENCODE project)[58], rabbit anti-HIM-8pT64 (1:2000)[41], and rabbit anti-RAD-51 (1:500)[37]. Secondary antibodies raised in donkeys were fluorescently labelled with Alexa Fluor® 488, Cy3 or Alexa Fluor® 647 (1:500, Jackson ImmunoResearch and Invitrogen). Gonads were mounted in ProLong Gold antifade mountant (ThermoFisher Scientific) and epifluorescence images were acquired on a DeltaVision Elite microscope (Applied Precision) using a 100× N.A. 1.4 oil-immersion objective.

For quantification of proteins levels by immunofluorescence, imaging was performed on a Marianas spinning-disk confocal microscope (3i) with a 100x 1.46 NA oil immersion objective. 3D stacks of wild-type (*syp-4-ha(ie29)*) and *syp-4(ie25)* animals were taken from the same slide and quantified in Fiji. SC containing voxels are identified by thresholding the SYP-2 and SYP-4-3xFlag channels for *syp-4(ie29)* and *syp-4(ie25)*, respectively. Images shown in Fig. S6 are background subtracted maximal intensity projections with equally scaled intensity values.

STORM and PALM imaging

30

511   Super-resolution imaging of dissected, immuno-stained intact germline tissue was carried out as

512   described[24]. Targets for STORM were labeled with donkey or goat secondary antibodies

513   labelled with Alexa Fluor® 647 (1:500, Jackson ImmunoResearch and Invitrogen).

514   Subsequently, the fluorescently tagged internal reference protein, mEos2-HIM-3 or mMaple3-

515   HIM-3[24] was imaged using PALM [59] [60]. For early pachytene images, mEos2-HIM-3 was

516   co-stained with a rabbit anti-HIM-3 antibody and a donkey-anti-rabbit secondary antibody

517   (Jackson ImmunoResearch) labelled with NHS esters of CF568 to achieve a 2:1 dye-to-antibody

518   ratio. Aligned and averaged images (Fig. S1) were used to generate histograms of localization

519   events in x and z[24]. To systematically distinguish between mono- and bi-modal distributions,

520   we evaluated fits with one and two Gaussians using an ANOVA test in R ($p < 0.05$). Standard

521   deviations of fit parameters were estimated by a subsampling approach using subsets of half the

522   number of individual SC stretches[24]. The results are summarized in Table S2.

523

524   **Statistical analysis**

525   Sample sizes were not predetermined, and experiments were not randomized. The investigators

526   were not blinded to allocation during experiments and outcome assessment. For STORM

527   experiments, the total lengths and number of stretches analyzed are summarized in Table S2.

528

529   **Analysis of of SC organization**

530   To derive a model for SC organization from our data, we asked which orientations of SC

531   proteins were consistent with the observed distributions, assuming that each protein is a rigid

532   rod. We first corrected the raw data by removing the extreme 2.5% of the localization events

533   using squared Mahalanobis distances in R (version 3.4.2). We then mapped each localization

534   event corresponding the nth-percentile in x and the mth-percentile in z of the N- (or C-) terminal

535   distribution to a randomly selected localization event within the nth ± 7.5% in x and mth ± 7.5%

536   in z of the corresponding C- (or N-) terminal distribution. This analysis reveals the distance

537   between the N- and C-terminal antibodies used for imaging and the orientation of the protein

538   within the SC. For further analysis, we remove outliers among the mapped localization events

539   with extreme values corresponding to the lower and upper 2.5% of distances.

540   To visualize changes within SC organization, we performed principal component analysis of the

541   widths, and – where applicable – positions off-center, for N- and C-terminal distributions of

31

542 SYP-1 and the C-terminal distribution of SYP-2, the orientations of SYP-1 molecules as

543 characterized by the median and 90th percentile angles, and the average distance between N- and

544 C-terminal antibodies using R (version 3.4.2). We excluded SYP-3 and SYP-4 from this analysis

545 since experimental challenges prevented us from analyzing their localizations for all genotypes.

546

547 **Recombination mapping**

548 To map meiotic recombination events, the *syp-4(ie25)* allele (generated in Bristol N2

549 background) was introgressed into the divergent Hawaiian strain CB4856 by 8 sequential crosses

550 and selection for *ie25*. Hawaiian and Bristol wild-type and *syp-4(ie25)* strains were crossed, and

551 the hybrid F1 progeny were backcrossed to Hawaiian males. These cross-progeny, which have

552 Hawaiian paternal chromosomes and recombined Bristol/Hawaiian maternal chromosomes, were

553 plated individually, allowed to reproduce for one generation, and the genomic DNA of their

554 pooled progeny was extracted by phenol-chloroform extraction. Illumina sequencing libraries

555 were prepared as described in [61] and sequenced as 50 bp single reads on a HiSeq2500 Illumina

556 sequencer at the Vincent J. Coates Genomics Sequencing Laboratory at UC Berkeley, with a

557 coverage of 2-4x per individual. Reads were mapped to the genomes of Bristol (Wormbase

558 release WS230) and Hawaiian[62] strains and genotypes called using the multiplexed shotgun

559 genotyping (MSG) toolbox and default parameters[63]. Aligned sequences obtained by deep

560 sequencing have been uploaded on the NCBI SRA database under accession number

561 SRP126693. Following this analysis, crossovers in oogenesis are characterized by transitions

562 from Hawaiian/Bristol heterozygous stretches to homozygous Hawaiian stretches, and the

563 calculated number of crossovers per nucleus is twice the number of mapped crossovers in the

564 oocytes.

565

566 **Electron microscopy**

567 High-pressure freezing, freeze-substitution, sample preparation, and microscopy was performed

568 as described previously[3, 64, 65]. Images were acquired on a Tecnai 12 transmission electron

569 microscope (120 kV, FEI, Hillsboro, OR) equipped with a Gatan Ultrascan 1000 CCD camera

570 (Pleasanton, CA).

571

32

Immunoblotting

To compare expression levels of SYP proteins, 120 adult worms were lysed by boiling in 40 µL Laemmli sample buffer (with β-mercaptoethanol) for about 5 min, until particulate matter was not detected using a dissection stereomicroscope. Samples of whole-worm lysates were run on a Nupage 4-12% polyacrylamide gradient gel and transferred to a PVDF membrane. Primary antibodies were rabbit (Pierce, PA1-985, used for HA-SYP-1) or mouse anti-HA (SYP-4-HA) and mouse anti-tubulin (EMD Millipore), each diluted 1:5,000. HRP-conjugated secondary antibodies (Jackson Laboratory) were detected with ECL reagents (Amersham). For SYP-4-HA blots, HA and tubulin were easily resolved and can be detected simultaneously. For HA-SYP-1, HA was detected by HRP-anti-rabbit/ECL and tubulin is detected by Cy3-conjugated anti-mouse secondary antibody (1:5,000). Images were recorded using a Chemidoc system (Bio-Rad) and quantified using Fiji.

Data Availability

NGS datasets generated during the current study are available on the NCBI SRA database under accession number SRP126693 (https://www.ncbi.nlm.nih.gov/sra/SRP126693). Any additional data are available upon reasonable request.

33

Competing Interests

The authors declare no competing interests.

Author Contributions

SK and MW performed experiments and analyzed data. SK, MW, KX and AFD designed experiments and wrote the manuscript.

References

1. Zickler D, Kleckner N (1999) Meiotic chromosomes: integrating structure and function. Annu Rev Genet 33:603–754. doi: 10.1146/annurev.genet.33.1.603

2. Moses MJ (1968) Synaptinemal complex. Annu Rev Genet 2:363–412.

3. Rog O, Köhler S, Dernburg AF (2017) The synaptonemal complex has liquid crystalline properties and spatially regulates meiotic recombination factors. Elife 6:e21455. doi: 10.7554/eLife.21455

34

621   4. Voelkel-Meiman K, Moustafa SS, Lefrançois P, et al (2012) Full-length synaptonemal

622   complex grows continuously during meiotic prophase in budding yeast. PLoS Genet

623   8:e1002993. doi: 10.1371/journal.pgen.1002993

624   5. Pattabiraman D, Roelens B, Woglar A, Villeneuve AM (2017) Meiotic recombination

625   modulates the structure and dynamics of the synaptonemal complex during C. elegans

626   meiosis. PLoS Genet 13:e1006670. doi: 10.1371/journal.pgen.1006670

627   6. Machovina TS, Mainpal R, Daryabeigi A, et al (2016) A Surveillance System Ensures

628   Crossover Formation in C. elegans. Curr Biol 26:2873–2884. doi: 10.1016/j.cub.2016.09.007

629   7. Nadarajan S, Lambert TJ, Altendorfer E, et al (2017) Polo-like kinase-dependent

630   phosphorylation of the synaptonemal complex protein SYP-4 regulates double-strand break

631   formation through a negative feedback loop. Elife 6:e23437. doi: 10.7554/eLife.23437

632   8. Hayashi M, Mlynarczyk-Evans S, Villeneuve AM (2010) The synaptonemal complex shapes

633   the crossover landscape through cooperative assembly, crossover promotion and crossover

634   inhibition during Caenorhabditis elegans meiosis. Genetics 186:45–58. doi:

635   10.1534/genetics.110.115501

636   9. Libuda DE, Uzawa S, Meyer BJ, Villeneuve AM (2013) Meiotic chromosome structures

637   constrain and respond to designation of crossover sites. Nature 502:703–706. doi:

638   10.1038/nature12577

639   10. Wang K, Wang C, Liu Q, et al (2015) Increasing the Genetic Recombination Frequency by

640   Partial Loss of Function of the Synaptonemal Complex in Rice. Mol Plant 8:1295–1298. doi:

641   10.1016/j.molp.2015.04.011

642   11. Woglar A, Villeneuve AM (2018) Dynamic Architecture of DNA Repair Complexes and the

643   Synaptonemal Complex at Sites of Meiotic Recombination. Cell 173:1678–1691.e16. doi:

644   10.1016/j.cell.2018.03.066

645   12. Cahoon CK, Helm JM, Libuda DE (2019) Synaptonemal complex proteins direct and

646   constrain the localization of crossover-promoting proteins during Caenorhabditis elegans

647   meiosis. bioRxiv 523605. doi: 10.1101/523605

648   13. Zhang L, Köhler S, Rillo-Bohn R, Dernburg AF (2018) A compartmentalized signaling

649   network mediates crossover control in meiosis. Elife 7:245. doi: 10.7554/eLife.30789

35

650   14. Dernburg AF, McDonald K, Moulder G, et al (1998) Meiotic recombination in C. elegans

651   initiates by a conserved mechanism and is dispensable for homologous chromosome

652   synapsis. Cell 94:387–398.

653   15. MacQueen AJ, Colaiácovo MP, McDonald K, Villeneuve AM (2002) Synapsis-dependent

654   and -independent mechanisms stabilize homolog pairing during meiotic prophase in C.

655   elegans. Genes Dev 16:2428–2442. doi: 10.1101/gad.1011602

656   16. Colaiácovo MP, MacQueen AJ, Martinez-Perez E, et al (2003) Synaptonemal complex

657   assembly in C. elegans is dispensable for loading strand-exchange proteins but critical for

658   proper completion of recombination. Dev Cell 5:463–474. doi: 10.1016/S1534-

659   5807(03)00232-6

660   17. Smolikov S, Eizinger A, Schild-Prüfert K, et al (2007) SYP-3 restricts synaptonemal

661   complex assembly to bridge paired chromosome axes during meiosis in Caenorhabditis

662   elegans. Genetics 176:2015–2025. doi: 10.1534/genetics.107.072413

663   18. Smolikov S, Schild-Prüfert K, Colaiácovo MP (2009) A yeast two-hybrid screen for SYP-3

664   interactors identifies SYP-4, a component required for synaptonemal complex assembly and

665   chiasma formation in Caenorhabditis elegans meiosis. PLoS Genet 5:e1000669. doi:

666   10.1371/journal.pgen.1000669

667   19. Schild-Prüfert K, Saito TT, Smolikov S, et al (2011) Organization of the synaptonemal

668   complex during meiosis in Caenorhabditis elegans. Genetics 189:411–421. doi:

669   10.1534/genetics.111.132431

670   20. Schücker K, Holm T, Franke C, et al (2015) Elucidation of synaptonemal complex

671   organization by super-resolution imaging with isotropic resolution. Proc Natl Acad Sci

672   112:2029–2033. doi: 10.1073/pnas.1414814112

673   21. Cahoon CK, Yu Z, Wang Y, et al (2017) Superresolution expansion microscopy reveals the

674   three-dimensional organization of theDrosophilasynaptonemal complex. Proc Natl Acad Sci

675   114:E6857–E6866. doi: 10.1073/pnas.1705623114

676   22. Rust MJ, Bates M, Zhuang X (2006) Sub-diffraction-limit imaging by stochastic optical

677   reconstruction microscopy (STORM). Nat Meth 3:793–795. doi: 10.1038/nmeth929

678   23. Huang B, Wang W, Bates M, Zhuang X (2008) Three-dimensional super-resolution imaging

679   by stochastic optical reconstruction microscopy. Science 319:810–813. doi:

680   10.1126/science.1153529

36

681 24. Köhler S, Wojcik M, Xu K, Dernburg AF (2017) Superresolution microscopy reveals the
682   three-dimensional organization of meiotic chromosome axes in intact Caenorhabditis elegans
683   tissue. Proc Natl Acad Sci 114:E4734–E4743. doi: 10.1073/pnas.1702312114
684 25. Zetka MC, Kawasaki I, Strome S, Müller F (1999) Synapsis and chiasma formation in
685   Caenorhabditis elegans require HIM-3, a meiotic chromosome core component that functions
686   in chromosome segregation. Genes Dev 13:2258–2270.
687 26. Gao J, Barroso C, Zhang P, et al (2016) N-terminal acetylation promotes synaptonemal
688   complex assembly in C. elegans. Genes Dev 30:2404–2416. doi: 10.1101/gad.277350.116
689 27. Schmekel K, Meuwissen RL, Dietrich AJ, et al (1996) Organization of SCP1 protein
690   molecules within synaptonemal complexes of the rat. Exp Cell Res 226:20–30. doi:
691   10.1006/excr.1996.0198
692 28. Sym M, Roeder GS (1995) Zip1-induced changes in synaptonemal complex structure and
693   polycomplex assembly. J Cell Biol 128:455–466.
694 29. Higgins JD, Sanchez-Moran E, Armstrong SJ, et al (2005) The Arabidopsis synaptonemal
695   complex protein ZYP1 is required for chromosome synapsis and normal fidelity of crossing
696   over. Genes Dev 19:2488–2500. doi: 10.1101/gad.354705
697 30. Meuwissen RL, Offenberg HH, Dietrich AJ, et al (1992) A coiled-coil related protein
698   specific for synapsed regions of meiotic prophase chromosomes. EMBO J 11:5091–5100.
699 31. Anderson LK, Royer SM, Page SL, et al (2005) Juxtaposition of C(2)M and the transverse
700   filament protein C(3)G within the central region of Drosophila synaptonemal complex. Proc
701   Natl Acad Sci USA 102:4482–4487. doi: 10.1073/pnas.0500172102
702 32. Rog O, Dernburg AF (2015) Direct Visualization Reveals Kinetics of Meiotic Chromosome
703   Synapsis. Cell Rep 10:1639–1645. doi: 10.1016/j.celrep.2015.02.032
704 33. Reynolds A, Qiao H, Yang Y, et al (2013) RNF212 is a dosage-sensitive regulator of
705   crossing-over during mammalian meiosis. Nat Genet 45:269–278. doi: 10.1038/ng.2541
706 34. Qiao H, Prasada Rao HBD, Yang Y, et al (2014) Antagonistic roles of ubiquitin ligase HEI10
707   and SUMO ligase RNF212 regulate meiotic recombination. Nat Genet 46:194–199. doi:
708   10.1038/ng.2858
709 35. de Gennes PG, Prost J (1993) The Physics of Liquid Crystals, 2nd ed. Clarendon Press,
710   Oxford

37

711   36. Yokoo R, Zawadzki KA, Nabeshima K, et al (2012) COSA-1 reveals robust homeostasis and

712   separable licensing and reinforcement steps governing meiotic crossovers. Cell 149:75–87.

713   doi: 10.1016/j.cell.2012.01.052

714   37. Harper NC, Rillo R, Jover-Gil S, et al (2011) Pairing centers recruit a Polo-like kinase to

715   orchestrate meiotic chromosome dynamics in C. elegans. Dev Cell 21:934–947. doi:

716   10.1016/j.devcel.2011.09.001

717   38. Sato-Carlton A, Nakamura-Tabuchi C, Chartrand SK, et al (2018) Phosphorylation of the

718   synaptonemal complex protein SYP-1 promotes meiotic chromosome segregation. The

719   Journal of Cell Biology 217:555–570. doi: 10.1083/jcb.201707161

720   39. Jantsch V, Pasierbek P, Mueller MM, et al (2004) Targeted gene knockout reveals a role in

721   meiotic recombination for ZHP-3, a Zip3-related protein in Caenorhabditis elegans. Mol Cell

722   Biol 24:7998–8006. doi: 10.1128/MCB.24.18.7998-8006.2004

723   40. Labella S, Woglar A, Jantsch V, Zetka M (2011) Polo kinases establish links between

724   meiotic chromosomes and cytoskeletal forces essential for homolog pairing. Dev Cell

725   21:948–958. doi: 10.1016/j.devcel.2011.07.011

726   41. Kim Y, Kostow N, Demburg AF (2015) The Chromosome Axis Mediates Feedback Control

727   of CHK-2 to Ensure Crossover Formation in C. elegans. Dev Cell 35:247–261. doi:

728   10.1016/j.devcel.2015.09.021

729   42. Hillers KJ, Villeneuve AM (2003) Chromosome-wide control of meiotic crossing over in C.

730   elegans. Curr Biol 13:1641–1647. doi: 10.1038/nrg1210

731   43. Nabeshima K, Villeneuve AM, Colaiácovo MP (2005) Crossing over is coupled to late

732   meiotic prophase bivalent differentiation through asymmetric disassembly of the SC. J Cell

733   Biol 168:683–689. doi: 10.1083/jcb.200410144

734   44. Broman KW, Weber JL (2000) Characterization of human crossover interference. Am J Hum

735   Genet 66:1911–1926. doi: 10.1086/302923

736   45. Muller HJ (1916) The mechanism of crossing-over IV. American Naturalist 50:421–434.

737   46. Drouaud J, Mercier R, Chelysheva L, et al (2007) Sex-specific crossover distributions and

738   variations in interference level along Arabidopsis thaliana chromosome 4. PLoS Genet

739   3:e106. doi: 10.1371/journal.pgen.0030106

740   47. Petkov PM, Broman KW, Szatkiewicz JP, Paigen K (2007) Crossover interference underlies
741   sex differences in recombination rates. Trends Genet 23:539–542. doi:
742   10.1016/j.tig.2007.08.015

743   48. Mets DG, Meyer BJ (2009) Condensins Regulate Meiotic DNA Break Distribution, thus
744   Crossover Frequency, by Controlling Chromosome Structure. Cell 139:73–86. doi:
745   10.1016/j.cell.2009.07.035

746   49. Zhang L, Liang Z, Hutchinson J, Kleckner N (2014) Crossover Patterning by the Beam-Film
747   Model: Analysis and Implications. PLoS Genet 10:e1004042. doi:
748   10.1371/journal.pgen.1004042

749   50. Goodyer W, Kaitna S, Couteau F, et al (2008) HTP-3 links DSB formation with homolog
750   pairing and crossing over during C. elegans meiosis. Dev Cell 14:263–274. doi:
751   10.1016/j.devcel.2007.11.016

752   51. Kleckner N, Zickler D, Jones GH, et al (2004) A mechanical basis for chromosome function.
753   Proc Natl Acad Sci USA 101:12592–12597. doi: 10.1073/pnas.0402724101

754   52. Brenner S (1974) The genetics of Caenorhabditis elegans. Genetics 77:71–94.

755   53. Frøkjær-Jensen C, Davis MW, Hopkins CE, et al (2008) Single-copy insertion of transgenes
756   in Caenorhabditis elegans. Nat Genet 40:1375–1383. doi: 10.1038/ng.248

757   54. Dickinson DJ, Ward JD, Reiner DJ, Goldstein B (2013) Engineering the Caenorhabditis
758   elegans genome using Cas9-triggered homologous recombination. Nat Meth 10:1028–1034.
759   doi: 10.1038/nmeth.2641

760   55. Redemann S, Schloissnig S, Ernst S, et al (2011) Codon adaptation-based control of protein
761   expression in C. elegans. Nat Meth 8:250–252. doi: 10.1038/nmeth.1565

762   56. Phillips CM, McDonald KL, Dernburg AF (2009) Cytological analysis of meiosis in
763   Caenorhabditis elegans. Methods Mol Biol 558:171–195. doi: 10.1007/978-1-60761-103-
764   5_11

765   57. Macqueen AJ, Phillips CM, Bhalla N, et al (2005) Chromosome sites play dual roles to
766   establish homologous synapsis during meiosis in C-elegans. Cell 123:1037–1050. doi:
767   10.1016/j.cell.2005.09.034

768   58. Gerstein MB, Lu ZJ, Van Nostrand EL, et al (2010) Integrative analysis of the
769   Caenorhabditis elegans genome by the modENCODE project. Science 330:1775–1787. doi:
770   10.1126/science.1196914

771   59. McKinney SA, Murphy CS, Hazelwood KL, et al (2009) A bright and photostable

772   photoconvertible fluorescent protein for fusion tags. Nat Meth 6:131–133. doi:

773   10.1038/nmeth.1296

774   60. Wang S, Moffitt JR, Dempsey GT, et al (2014) Characterization and development of

775   photoactivatable fluorescent proteins for single-molecule-based superresolution imaging.

776   Proc Natl Acad Sci 111:8452–8457. doi: 10.1073/pnas.1406593111

777   61. Meyer M, Kircher M (2010) Illumina sequencing library preparation for highly multiplexed

778   target capture and sequencing. Cold Spring Harb Protoc 2010:pdb.prot5448. doi:

779   10.1101/pdb.prot5448

780   62. Thompson OA, Snoek LB, Nijveen H, et al (2015) Remarkably Divergent Regions Punctuate

781   the Genome Assembly of the Caenorhabditis elegans Hawaiian Strain CB4856. Genetics

782   200:975–989. doi: 10.1534/genetics.115.175950

783   63. Andolfatto P, Davison D, Erezyilmaz D, et al (2011) Multiplexed shotgun genotyping for

784   rapid and efficient genetic mapping. Genome Res 21:610–617. doi: 10.1101/gr.115402.110

785   64. McDonald KL, Webb RI (2011) Freeze substitution in 3 hours or less. J Microsc 243:227–

786   233. doi: 10.1111/j.1365-2818.2011.03526.x

787   65. McDonald KL (2014) Rapid embedding methods into epoxy and LR White resins for

788   morphological and immunological analysis of cryofixed biological specimens. Microsc

789   Microanal 20:152–163. doi: 10.1017/S1431927613013846

790

791